applied sciences

MDPI

Article

A Single-End Location Method for Small Current Grounding System Based on the Minimum Comprehensive Entropy Kurtosis Ratio and Morphological Gradient

Jiyuan Cao [1], Yanwen Wang [1], Lingjie Wu [2], Yongmei Zhao [3] and Le Wang [4,*]

[1] School of Mechanical and Electrical Engineering, China University of Mining and Technology-Beijing, Beijing 100083, China; bqt2100403013@student.cumtb.edu.cn (J.C.); wyw@cumtb.edu.cn (Y.W.)
[2] Petrochina Planning and Engineering Institute, Beijing 100083, China; wulingjie@petrochina.com.cn
[3] Technical and Economic Research Institute, The CHN Energy, Beijing 100083, China; 20035055@ceic.com
[4] Datang North China Electric Power Test and Research Institute, China Datang Corporation Science and Technology General Research Institute Co., Ltd., Beijing 100043, China
* Correspondence: wangle249@126.com

Abstract: Fault location technology is crucial for enhancing the efficiency of fault maintenance and ensuring the safety of the power supply in small current grounding systems. To address the challenge that traditional single-end positioning methods experience when identifying the reflected wave head and that the adaptability of wave head calibration methods is typically limited, a single-end location method of modulus wave velocity differences based on marine predator algorithm optimized multivariate variational mode decomposition (MVMD) and morphological gradient is proposed. Firstly, the minimum comprehensive entropy kurtosis ratio is used as the fitness function, and the marine predator algorithm is used to realize the automatic optimization of the mode number and penalty factor of the multivariate variational mode decomposition. Therefore, with the goal of decomposing the traveling wave characteristic signals with the most significant traveling wave characteristic information and the lowest noise component, the line-mode traveling wave and the zero-mode traveling wave are accurately decomposed. Secondly, the intrinsic mode function component with the smallest entropy kurtosis ratio is selected as the line-mode traveling wave characteristic signal and the zero-mode traveling wave characteristic signal, respectively, and the arrival time of the wave head is accurately calibrated by combining the morphological gradient value. Finally, the fault distance is calculated by the modulus wave velocity difference location formula and compared with the variational mode decomposition-Teager energy operator (VMD-TEO) method and the empirical mode decomposition _first-order difference method. The results show that the proposed method has the highest accuracy of positioning results, and the algorithm time is significantly reduced compared with the VMD-TEO method, and it has strong adaptability to different line types of faults, different fault initial conditions, and noise interference.

Keywords: fault location; multivariate variational mode decomposition; small current grounding systems; marine predator algorithm; modulus wave velocity difference

check for updates

Academic Editor: Len Gelman

Received: 13 February 2025
Revised: 20 March 2025
Accepted: 21 March 2025
Published: 24 March 2025

Citation: Cao, J.; Wang, Y.; Wu, L.; Zhao, Y.; Wang, L. A Single-End Location Method for Small Current Grounding System Based on the Minimum Comprehensive Entropy Kurtosis Ratio and Morphological Gradient. *Appl. Sci.* **2025**, *15*, 3539. https://doi.org/10.3390/app15073539

Copyright: © 2025 by the authors. Licensee MDPI, Basel, Switzerland. This article is an open access article distributed under the terms and conditions of the Creative Commons Attribution (CC BY) license (https://creativecommons.org/licenses/by/4.0/).

1. Introduction

In China's medium and low voltage power distribution networks, small current grounding systems are extensively implemented [1]. Single-phase Earth faults constitute approximately 70% of all electrical malfunctions. When such faults occur, the phase voltage of the non-fault phase escalates to $\sqrt{3}$ times its initial value. Delayed fault resolution

may lead to substantial equipment deterioration or pose significant safety risks. Hence, developing precise and dependable fault localization techniques is crucial for enhancing maintenance capabilities and ensuring power distribution reliability [2].

At present, fault localization techniques primarily encompass three methodologies: the traveling wave method, the impedance method [3,4], and signal injection approaches [5,6]. The traveling wave method has garnered particular attention due to its minimal susceptibility to variables such as fault transition resistance and system operation mode. This method branches into two categories mainly: single-end methods and double-end methods. While double-end methods offer reliable initial wave head detection, their accuracy heavily depends on precise clock synchronization between endpoints and requires additional terminal ranging equipment, resulting in elevated implementation costs. Although single-end methods [7] present cost advantages and eliminate synchronization requirements, they face challenges in accurately identifying the reflected wave head due to adjacent line interference and impedance variations. To address these limitations, reference [8] introduced an innovative ranging technique leveraging zero-mode and line-mode wave velocity differentials. This approach only requires initial wave head detection in both modes, offering enhanced reliability through simplified principles. Reference [9] developed constraint relationships between zero–line-mode temporal differences, velocity disparities, and transmission distances, utilizing particle swarm optimization (PSO) to determine optimal fault locations. Reference [10] further refined this methodology by implementing an enhanced truncation error correction algorithm.

The accurate detection of traveling wave characteristics and wave head identification remains a significant technical challenge. Research [11] employed db4 mother wavelet's initial decomposition scale for traveling wave head extraction. While wavelet transform-based multi-resolution analysis effectively identifies traveling wave singularities, the effectiveness of fault feature extraction heavily depends on decomposition parameters and wavelet basis selection. Addressing these limitations, reference [12] developed an alternative approach combining empirical mode decomposition (EMD) with fast Fourier transform (FFT). Though EMD eliminates the need for wavelet basis and scale selection, it suffers from significant modal aliasing and boundary effects. To overcome these challenges, reference [13] introduced a methodology utilizing variational mode decomposition (VMD) alongside Teager energy operator (TEO) for wave head calibration. The multivariate variational mode decomposition (MVMD) extends VMD's capabilities from single to multiple dimensions, maintaining resistance to modal aliasing while efficiently processing multivariable data, thus enabling faster fault localization. Reference [14] introduced a novel wave head identification technique incorporating MVMD and kurtosis measurements, utilizing kurtosis values to calibrate high-frequency traveling wave signals post-MVMD. However, this method's accuracy is notably influenced by the modal decomposition parameter K and penalty coefficient α. Reference [15] addressed this by developing a comprehensive metric incorporating correlation coefficients, residual signal permutation entropy, and instantaneous energy loss ratios to optimize these parameters. Nevertheless, this optimization process remains complex and requires recalibration when line parameters or initial fault conditions shift, limiting the algorithm's adaptability.

To address these persistent challenges in current traveling wave positioning methodologies, this paper presents an innovative single-end positioning approach that combines marine predator algorithm (MPA)-optimized MVMD with morphological gradient analysis. Firstly, the generation principle of traveling waves and phase-mode transformation is introduced. Secondly, a wave head calibration method based on parameter optimization MVMD and morphological gradient is proposed. Then, the fault location formulas under single line and mixed line are proposed. Finally, the influence of line type, initial fault

condition, and noise on the proposed method is verified by simulation and compared with different algorithms. The research focuses on the following three key aspects:

(1) MPA considers that the minimum comprehensive entropy kurtosis ratio is introduced to optimize the decomposition mode number K and penalty factor α of MVMD. The MVMD algorithm optimized by MPA can decompose the traveling wave characteristic signals with the most significant singularity and the lowest noise component as the target, so as to accurately decompose the line-mode traveling wave and the zero-mode traveling wave.
(2) Compared with the independent processing of the two traveling waves, only one parameter optimization and one MVMD are needed, which effectively shortens the extraction time of traveling wave characteristic signals while retaining the advantages of VMD noise interference robustness and is not affected by modal aliasing.
(3) Focusing on the problem of large positioning error caused by inconsistent wave velocity of hybrid line in small current grounding system, an equivalent method based on modulus wave velocity ratio is proposed. The hybrid line is equivalent to a single line for ranging, which effectively improves the accuracy of positioning results.

2. Traveling Wave Principle and Phase-Mode Transformation

The generation of a traveling wave can be analyzed by the superposition principle, as shown in Figure 1, assuming that the voltage of a certain point F of the power supply cable is normal when the voltage is $\dot{U}_F$. After the ground fault occurs at this point, point F has the same potential as the Earth, and the switch K is closed. Point F is equivalent to superimposing an additional power supply $-\dot{U}_F$ with the same voltage and opposite direction when the point is normal. Under the action of additional power supply $-\dot{U}_F$, point F will produce traveling wave signals transmitted to both ends.

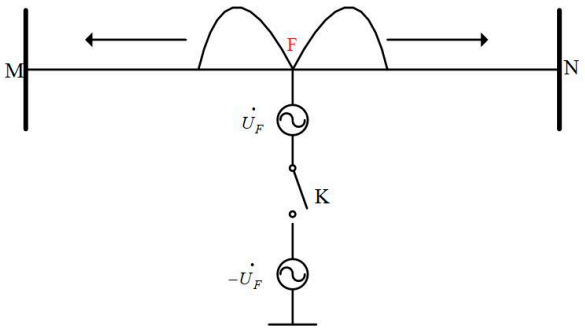


Figure 1. Principal diagram of traveling wave generation.

The specific traveling wave transmission process is expressed by the wave equation, as shown in Equation (1).

$$\begin{cases} \frac{\partial^2 U}{\partial x^2} = LC\frac{\partial^2 U}{\partial t^2} \\ \frac{\partial^2 I}{\partial x^2} = CL\frac{\partial^2 I}{\partial t^2} \end{cases} \quad (1)$$

Within the equations, U and I represent the phase-to-ground voltage and conductor line current, respectively, while x denotes the line length and t signifies time. The per-unit-length parameters L and C correspond to the inductance and capacitance parameter matrices along the transmission line. The electromagnetic coupling between three-phase conductors results in non-diagonal L and C matrices, making direct equation solving highly complex. To simplify the analytical and computational process, phase-mode transformation is applied to diagonalize L, C, LC, and CL matrices. This study employs Karenbauer trans-

formation to accomplish the phase-mode conversion of the traveling wave, as expressed in Equation (2).

$$\begin{bmatrix} u_0 \\ u_1 \\ u_2 \end{bmatrix} = \frac{1}{3} \begin{bmatrix} 1 & -1 & 0 \\ 1 & 0 & -1 \\ 1 & 1 & 1 \end{bmatrix} \begin{bmatrix} u_A \\ u_B \\ u_C \end{bmatrix} \tag{2}$$

In the formula, u_0 is a zero-mode traveling wave, which forms a loop through the Earth. u_1 and u_2 are line-mode traveling waves, which form a loop through two non-fault phases. u_A, u_B, and u_C are three-phase voltages.

After phase-mode transformation, the lines are decoupled, and the wave equation is shown in Formula (3).

$$\begin{cases} \frac{\partial^2 U_m}{\partial x^2} = \Lambda_u \frac{\partial^2 U_m}{\partial t^2} \\ \frac{\partial^2 I_m}{\partial x^2} = \Lambda_u \frac{\partial^2 I_m}{\partial t^2} \end{cases} \tag{3}$$

In the formula, Λ_u is the modulus diagonal matrix after matrix transformation.

Thus, the D'Alembert form general solution of the modulus voltage and current at any time and place is shown in Formula (4).

$$\begin{cases} u_m(x,t) = u_m^+(t - x/c_m + \alpha_m^+) + u_m^-(t + x/c_m + \alpha_m^-) \\ i_m(x,t) = i_m^+(t - x/c_m + \alpha_m^+) + i_m^-(t + x/c_m + \alpha_m^-) \end{cases} \tag{4}$$

In the formula, α_m^+ and α_m^- are arbitrary constants, where both the forward traveling wave u_m^+ and the reverse traveling wave u_m^- can be arbitrary functions. The modulus wave velocity formula of each modulus is shown in Formula (5).

$$v_m = \frac{1}{\sqrt{L_m C_m}} \tag{5}$$

Equation (5) demonstrates that line-mode and zero-mode traveling waves propagate at distinct velocities due to their different transmission channel parameters, resulting in varying arrival times at the measurement point. This velocity differential between modes enables fault location determination. A key advantage of this approach is that it only requires detection of the initial wave heads for both line-mode and zero-mode traveling waves, thus circumventing the challenges associated with identifying reflected wave signatures.

3. Wave Head Calibration Based on Parameter Optimization MVMD and Morphological Gradient

3.1. MVMD

MVMD was first proposed by Rehman et al. [16] in 2019. It is a multivariate extension of a novel VMD. Compared with traditional VMD, MVMD can process signals of multiple channels at the same time. In order to minimize the sum of the bandwidth of all intrinsic mode functions on all channels, and the sum of each mode can accurately recover the original signal, the correlation between each channel is fully utilized to improve the accuracy of signal decomposition and shorten the time of fault feature extraction, so as to quickly realize fault location [17]. In this paper, MVMD is used to decompose line-mode voltage and zero-mode voltage at the same time. The specific steps are as follows:

Suppose that both the line-mode voltage and the zero-mode voltage are decomposed into m intrinsic mode function (IMF) components, as shown in (6).

$$x_c(t) = \sum_{i=1}^{m} u_m(t), \quad c = 1, 0 \tag{6}$$

In the formula, $x_c(t) = [x_1(t), x_0(t)]$, $x_1(t)$ is the line-mode voltage signal, and $x_0(t)$ is the zero-mode voltage signal. $u_m(t) = [u_1(t), u_2(t), \ldots, u_m(t)]$ and $u_m(t)$ are the mth IMF component.

The Hilbert transform is performed on the component $u_m(t)$ to obtain the analytical representation of the vector, which is denoted as $u_+^m(t)$, and the bandwidth of each mode $u_+^m(t)$ is estimated by the L_2 norm square of the gradient function after the harmonic conversion. Then, the related optimization problem under the constraint condition is changed into Formula (7).

$$\begin{aligned} &\min_{\{u_{m,c}\},\{\omega_m\}} \left\{ \sum_m \sum_c \left\| \partial_t \left[u_+^{m,c}(t) e^{-j\omega_m t} \right] \right\|_2^2 \right\} \\ &s.t. \sum_m u_{m,c}(t) = x_c(t), c = 1, 2, \ldots, C \end{aligned} \tag{7}$$

In the formula, $u_+^{m,c}(t)$ denotes the corresponding channel c and the analytic signal with mode m. ω_m denotes the central frequency of the mth mode, and ∂_t denotes the time-dependent partial derivative.

By introducing the Lagrange multiplication operator, (7) is transformed from a constrained problem to an unconstrained problem, and the corresponding augmented Lagrange expression is shown in (8).

$$\begin{aligned} &\mathcal{L}\left(\{u_{k,c}\}, \{\omega_k\}, \lambda_c\right) = \alpha \sum_k \sum_c \left\| \partial_t \left[u_+^{k,c}(t) \mathrm{e}^{-\mathrm{j}\omega_k t} \right] \right\|_2^2 + \\ &\sum_c \left\| x_c(t) - \sum_k u_{k,c}(t) \right\|_2^2 + \sum_c \left\langle \lambda_c(t), x_c(t) - \sum_k u_{k,c}(t) \right\rangle \end{aligned} \tag{8}$$

In Formula (8), $\langle \cdot \rangle$ presents the inner product. Finally, the above unconstrained problem is solved by the alternating direction multiplier algorithm, and the center frequency update is expressed as (9), so as to complete the adaptive decomposition of multivariate signals through the updated relationship.

$$\omega_k^{n+1} = \frac{\sum_c \int_0^\infty \omega \left| \hat{u}_{k,c}(\omega) \right|^2 d\omega}{\sum_c \int_0^\infty \left| \hat{u}_{k,c}(\omega) \right|^2 d\omega} \tag{9}$$

3.2. MPA

MPA is an optimization meta-heuristic optimization algorithm that explores the optimal solution by simulating the predation behavior between predators and prey [18]. It is inspired by the efficient predation strategy of marine organisms.

In the framework of MPA, the ocean is regarded as the global search space of the optimization problem, and the elite predator matrix represents the set of optimal solutions found in this space. At the same time, the prey matrix records the optimal candidate solutions obtained in the current iteration rounds. Based on the principle of complex interaction between predators and prey, the iterative process of MPA covers three core links: population initialization, iterative optimization, and marine memory update. Regarding the specific details of these processes, readers can refer to the literature [18], as this article will not be discussed here.

Permutation entropy serves as a quantitative measure for evaluating time series signals' randomness and complexity, distinguished by its computational efficiency and robust resistance to interference [19]. The magnitude of permutation entropy correlates directly with the complexity of traveling wave intrinsic mode function components—higher entropy values indicate greater complexity and noise content. To optimize wave head calibration

accuracy, the intrinsic mode function component exhibiting the lowest permutation entropy is selected as the traveling wave characteristic signal, effectively minimizing noise-induced influence. The permutation entropy calculation proceeds through the following steps:

The phase space reconstruction of the mth traveling wave intrinsic mode function component $\{\mathrm{IMF}_m(n), n = 1, 2, \cdots, N\}$ is carried out, and Formula (10) is obtained.

$$\begin{pmatrix} \mathrm{IMF}_m(1) & \mathrm{IMF}_m(1+\tau) & \cdots & \mathrm{IMF}_m(1+(q-1)\tau) \\ \mathrm{IMF}_m(2) & \mathrm{IMF}_m(2+\tau) & \cdots & \mathrm{IMF}_m(2+(q-1)\tau) \\ \mathrm{IMF}_m(n) & \mathrm{IMF}_m(n+\tau) & \cdots & \mathrm{IMF}_m(j+(q-1)\tau) \\ \vdots & \vdots & & \vdots \\ \mathrm{IMF}_m(K) & \mathrm{IMF}_m(K+\tau) & \cdots & \mathrm{IMF}_m(K+(q-1)\tau) \end{pmatrix} \tag{10}$$

In the formula, $n = 1, 2, \cdots, K$, q is the embedding dimension, and τ is the delay time.

Each reconstructed component $\{\mathrm{IMF}_m(n), \mathrm{IMF}_m(n+\tau), \cdots, \mathrm{IMF}_m(n+(q-1)\tau)\}$ is arranged in ascending order according to its size, and Formula (11) is obtained.

$$\mathrm{IMF}_m(i+(n_1-1)\tau) \leqslant \cdots \leqslant \mathrm{IMF}_m\left(i+\left(n_q-1\right)\tau\right) \tag{11}$$

Here, $n_1, n_2, \cdots, n_q$ is the column of the elements in the reconstructed component.

For each row of the matrix obtained by reconstructing the intrinsic mode function component $\mathrm{IMF}_m(n)$, a set of symbol sequences can be obtained, as shown in Formula (12).

$$S(l) = \left(n_1, n_2, \cdots, n_q\right) \tag{12}$$

In the formula, $l = 1, 2, \cdots, k$, and $k \leqslant q!$. There are a total of $q!$ different symbol sequences $\left(n_1, n_2, \cdots, n_q\right)$ of q-dimensional phase space mapping, and the symbol sequence $S(l)$ is one of the permutations. If the probabilities of k different symbol sequences are $P_1, P_2, \cdots, P_k$, then the permutation entropy can be expressed as shown in Formula (13).

$$H_P(q) = -\sum_{n=1}^{k} P_n \ln P_n \tag{13}$$

The permutation entropy H_{pm} of the mth traveling wave intrinsic mode function component can be obtained by normalizing it, as shown in Formula (14).

$$H_{Pm} = H_P / \ln(q!) \tag{14}$$

The kurtosis value is a dimensionless parameter to measure the kurtosis of signal waveform, which can effectively describe the mutability of complex signals [20]. The kurtosis value of the signal obeying the normal distribution is about 3, while the singularity of the traveling wave fault characteristic signal is significant and obviously deviates from the normal distribution, and its kurtosis value should be greater than 3. The larger the kurtosis value of the intrinsic mode function component, the richer the traveling wave characteristic information. The formula for calculating the kurtosis value k_m of the mth intrinsic mode function component obtained by MVMD is shown in Formula (15).

$$k_m = \frac{\sum_{n=1}^{N} \left[\mathrm{IMF}_m(n) - \mu_{\mathrm{IMF}_m}\right]^4}{(N-1)\sigma^4{}_{\mathrm{IMF}_m}} \tag{15}$$

In the formula, $\mathrm{IMF}_m(n)$ is the mth intrinsic mode function component obtained by decomposing the traveling wave signal by MVMD. μ_{IMF_m}, σ_{IMF_m}, and N are the

mean value, standard deviation, and the number of sampling points of the IMF_m component, respectively.

3.3. Traveling Wave Characteristic Signal Extraction Based on MPA-Optimized MVMD

According to the basic principle of MVMD, when using MVMD to decompose line-mode voltage and zero-mode voltage, it is necessary to set the number of intrinsic mode functions K and penalty factor α in advance. K and α determine the accuracy and bandwidth of modal decomposition, which directly affects the extraction effect of traveling wave characteristic signals. At present, it is common to set two core parameters based on human experience, but the randomness and uncertainty of human setting will inevitably have a certain impact on the correctness of MVMD results. Through multiple iterations, MPA gradually converges to the optimal solution, that is, the predator position with the highest fitness, so as to realize the search and optimization of the core parameters. In this paper, the optimal number of modes $\hat{K}$ and penalty factors $\hat{\alpha}$ of MVMD are obtained by MPA. The specific optimization steps are shown in Figure 2.

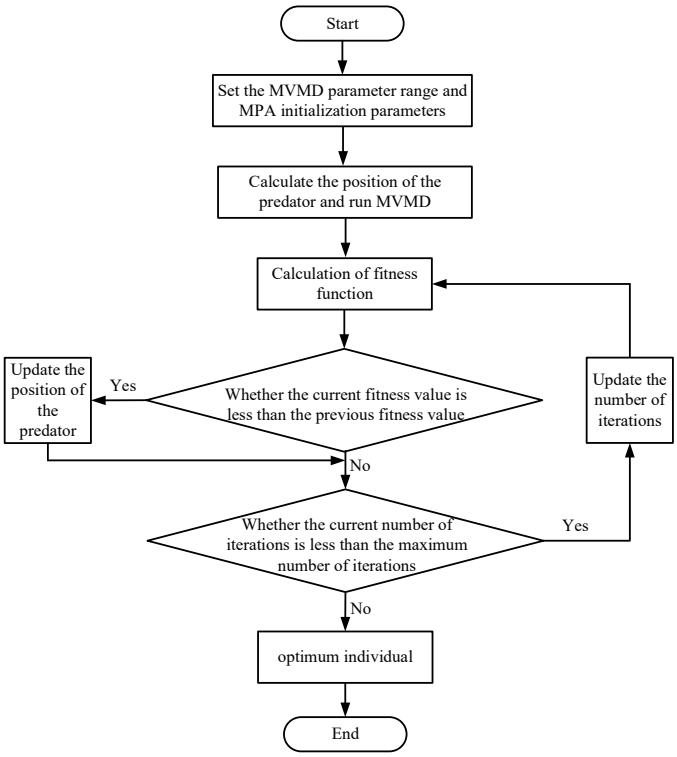


Figure 2. MPA-optimized MVMD flow chart.

The MPA fitness function is constructed based on minimizing the comprehensive entropy kurtosis ratio of both line-mode and zero-mode traveling waves, as expressed in Formula (16).

$$\langle \hat{K}, \hat{\alpha} \rangle = \mathrm{argmin}_{(K,\alpha)} \left\{ \sum_{c} \min_{\{x_c\}} \left\{ \frac{H_{Pm}}{k_m - 3} \right\} \right\} \tag{16}$$

Within this formula, $\mathrm{argmin}_{(K,\alpha)}(\cdot)$ yields the parameter values corresponding to the function's minimum value, with $\hat{K}$ and $\hat{\alpha}$ representing the optimal parameter. $x_c(t)$ denotes the combined set of line-mode and zero-mode voltage signals. The permutation entropy value of the mth traveling wave intrinsic mode function component is represented by H_{Pm}, while k_m indicates the kurtosis value of the mth intrinsic mode function component.

Formula (16) demonstrates that the fitness function, founded on minimizing the comprehensive entropy kurtosis ratio, enables MVMD to simultaneously decompose both

line-mode and zero-mode voltage signals while targeting the extraction of traveling wave characteristic signals that contain the most significant wave information and minimal noise components.

Subsequently, the IMF component exhibiting the lowest entropy/kurtosis ratio among all IMFs from line-mode voltage decomposition is defined as the line-mode traveling wave characteristic signal. Similarly, the IMF with the minimum entropy/kurtosis ratio from zero-mode voltage decomposition is defined as the zero-mode traveling wave characteristic signal, thus completing the extraction of the traveling wave characteristic signals.

3.4. Morphological Gradient

In order to highlight the amplitude mutation characteristics of the traveling wave signal, the morphological gradient [21] is introduced. The basic idea is to use the flat structural element-like 'probe' to perform expansion and corrosion operations in the mathematical morphology of the traveling wave signal, and to highlight the change area in the traveling wave signal by calculating the difference. The steps of using morphological gradient to calibrate the arrival time of the wave head are as follows:

For the traveling wave signal $x(t)$, its definition domain is D_x, and for the flat structure element $g(p)$, its definition domain is D_g, which this paper selects as 3, with the expansion calculation formula shown in (17) and the corrosion calculation formula shown in (18).

$$(x \oplus g)(t) = \max_{m \in D_g}(x(t-p) + g(p)), (t-p) \in D_x \quad (17)$$

$$(x \ominus g)(t) = \min_{m \in D_g}(x(t+p) - g(p)), (t+p) \in D_x \quad (18)$$

The morphological gradient calculation formula is shown in (19).

$$G(t) = (x \oplus g)(t) - (x \ominus g)(t) \quad (19)$$

The corresponding time of the maximum morphological gradient $G_{\max}(t)$ is the arrival time of the wave head.

Analysis of Formula (19) reveals that morphological gradient computation involves only basic mathematical operations—addition, subtraction, and extremum determination. This computational simplicity yields high execution efficiency and avoids complex integral transformations while maintaining robust resistance to noise interference. The method's calculation of differences between local maxima and minima makes it particularly sensitive to traveling wave signal mutation points, making it well suited for determining wave head arrival times.

4. Fault Location Principle

Due to the distinct velocities of line-mode and zero-mode traveling waves in overhead lines versus cables, separate positioning formulas are required for single line and hybrid line scenarios, as illustrated in Figure 3. The voltage traveling wave ranging device is installed at section M, with MN representing a cable line section and MT representing a hybrid line section. Cable lines are shown in black solid lines, while overhead lines are shown in gray. The wave velocities are represented as follows: v_0 and v_1 indicate the zero-mode and line-mode traveling wave velocities in the cable lines, respectively, while v_{h0} and v_{h1} denote the corresponding velocities in the overhead lines.

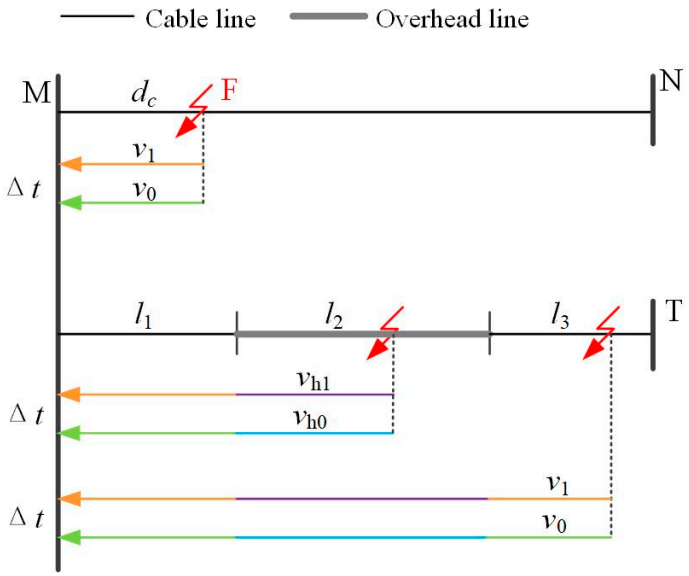


Figure 3. Traveling wave propagation diagram.

4.1. Single Line Positioning Formula

At point F on the MN line, a single-phase ground fault occurs. The traveling wave ranging device at section M measures the modal time difference Δt_R between the line-mode and zero-mode waves, while d_c represents the distance from point F to section M. With t_1 and t_0 denoting the arrival times of line-mode and zero-mode traveling wave heads at the M section ranging device, respectively, Formulas (20) and (21) are known.

$$\begin{cases} t_{R1} = \frac{d_c}{v_1} \\ t_{R0} = \frac{d_c}{v_0} \end{cases} \tag{20}$$

$$\Delta t_R = t_{R0} - t_{R1} = \frac{(v_1 - v_0)}{v_0 v_1} d_c \tag{21}$$

In a single cable line, the distance between the fault point and the ranging device is shown in Formula (22).

$$d_c = \frac{v_0 v_1}{v_1 - v_0} \Delta t_R \tag{22}$$

4.2. Hybrid Line Positioning Formula

When a single-phase grounding fault occurs at any point on the MT line, the zero-mode time difference in the line-mode measured by the M section ranging device is Δt_R. In this paper, the hybrid line is equivalent to a single cable line for fault location. The specific steps are as follows:

Firstly, the overhead line is equivalent to a cable line, and the equivalent proportional coefficient r is given, as shown in Formula (23). According to the distance of each section in the hybrid line, the equivalent single line section distance l_{mi} is given, as shown in Formula (24).

$$r = \frac{v_1 v_0}{v_1 - v_0} / \frac{v_{h0} v_{h1}}{v_{h1} - v_{h0}} \tag{23}$$

$$l_{mi} = \begin{cases} r l_i, & \text{if } i \text{ is overhead line section} \\ l_i, & \text{if } i \text{ is cable section} \end{cases} \tag{24}$$

Secondly, according to Formula (22), the fault distance d_c of the equivalent single line is obtained, and the fault section is judged to be the overhead line section or the cable section according to the equivalent single line section l_{mi} distance.

Finally, through Formula (25), the equivalent single line fault distance d_c is converted to the hybrid line fault distance d_h.

$$d_h = \begin{cases} \frac{d_c - \sum_{i=1}^{i-1} l_{mi}}{r} + \sum_{i=1}^{i-1} l_i, \text{ the fault section is overhead line section} \\ d_c - \sum_{i=1}^{i-1} l_{mi} + \sum_{i=1}^{i-1} l_i, \text{ the fault section is cable section} \end{cases} \quad (25)$$

4.3. Fault Location Process

Combined with the above analysis, The positioning flow chart is shown in Figure 4. The fault location process of this paper is as follows:

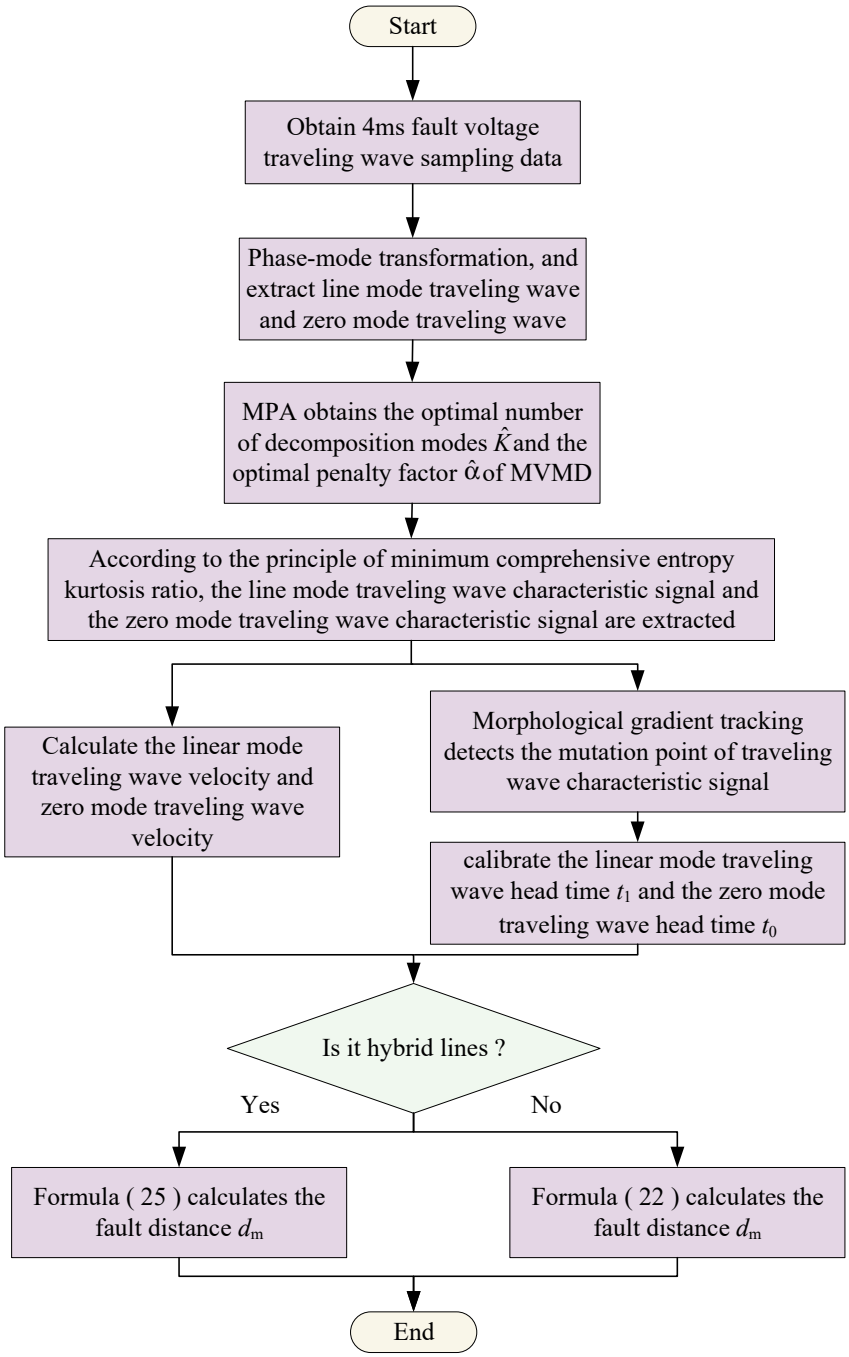


Figure 4. Positioning flow chart.

1. The time-domain voltage traveling wave waveform from 1 ms before the fault to 3 ms after the fault is intercepted, and the line-mode traveling wave and zero-mode traveling wave are extracted by the phase-mode transformation shown in Formula (2).
2. The optimal decomposition mode number $\hat{K}$ and optimal penalty factor $\hat{\alpha}$ of MVMD are obtained by MPA optimization algorithm considering the minimum comprehensive entropy kurtosis ratio.
3. The MVMD is used to simultaneously decompose the line-mode traveling wave and the zero-mode traveling wave, and the IMF with the smallest entropy/kurtosis ratio is extracted as the line-mode traveling wave characteristic signal and the zero-mode traveling wave characteristic signal, respectively.
4. The wave head calibration of the traveling wave characteristic signal is carried out by the morphological gradient, and the arrival time t_1 of the linear mode traveling wave head and the arrival time t_0 of the zero-mode traveling wave head are obtained.
5. The line-mode traveling wave velocity and zero-mode traveling wave velocity are calculated by Formula (5). If it is a single cable line, the fault distance d_m is calculated by Formula (22). If it is a hybrid line, the fault distance d_m is calculated by Formula (25).

5. Simulation Verification

To validate the accuracy of our proposed single-end ranging method, a simulation model of a 10 kV small current grounding system using MATLAB/Simulink is built, with the topology illustrated in Figure 5. The model incorporates voltage traveling wave measuring devices positioned at section M, with black solid lines representing cable lines and gray solid lines indicating overhead lines. The system contains five main feeders (from top to bottom: main feeder l_1, . . ., main feeder l_5). The main feeder l_5 is an overhead line-cable hybrid structure. The length of each line is marked in Figure 5. The line parameter table is shown in Table 1. The sampling frequency of the system is 1 MHz, and the total simulation time is 0.5 s.

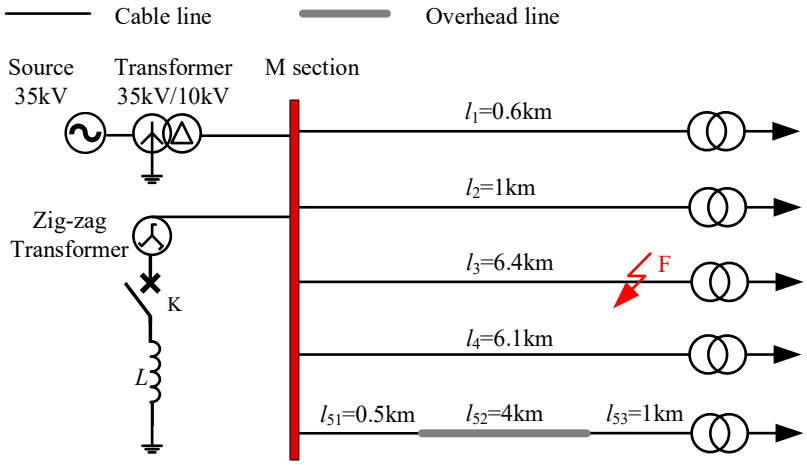


Figure 5. Simulation model of 10 kV small current grounding system.

Table 1. Line parameter table.

line Type	Phase Sequence	*R*/Ω	L/mH	C/μF
overhead line	positive sequence	0.17	1.21	0.09
	zero sequence	0.23	5.48	0.05
cable line	positive sequence	0.11	0.52	0.29
	zero sequence	0.34	1.54	0.19

Despite the complex topology of small current grounding systems, their typical length remains relatively modest, generally not exceeding 10–20 km. Drawing from reference [22], which establishes a monotonic relationship between zero-mode detection wave velocity and fault distance, the zero-mode wave velocity can be considered to be constant in the small current grounding system. Consequently, the constant parameter model (5) is employed to calculate both line-mode and zero-mode wave velocities. Using the parameters specified in Table 1, the wave velocities for both overhead lines and cable lines are computed according to Formulas (26) and (27).

$$\begin{cases} v_0 = 0.5846 \times 10^5 \text{km/s} \\ v_1 = 0.8143 \times 10^5 \text{km/s} \end{cases} \tag{26}$$

$$\begin{cases} v_{h0} = 1.7452 \times 10^5 \text{km/s} \\ v_{h1} = 2.9212 \times 10^5 \text{km/s} \end{cases} \tag{27}$$

5.1. The Influence of Line Type

(1) A test scenario was configured with a single-phase ground fault occurring 5.2 km from section M on cable line l_3 at 0.135 s, using parameters of 10 Ω grounding resistance and 270° initial fault phase angle.

Initially, MPA was employed to optimize MVMD core parameters using Equation (16), guided by the minimum comprehensive entropy kurtosis ratio principle for both wave modes. To validate MPA's effectiveness, PSO and the Sparrow Search Algorithm (SSA) are used for comparative analysis, averaging results across 10 experimental iterations. To ensure fair comparison, consistent parameters were applied across all three algorithms: population size of 30, maximum iterations of 15, mode number (K) search range [2, 10], and quadratic penalty factor (α) range [50, 10,000]. Algorithm-specific parameters were configured as follows: for PSO, individual and social learning factors were set to 1.5; for SSA, safety threshold (ST) = 0.7, with discoverers comprising 30% of population and alerters 50%; for MPA, the fish aggregation device effect coefficient was set to 0.2. The comparative results are illustrated in Figure 6.

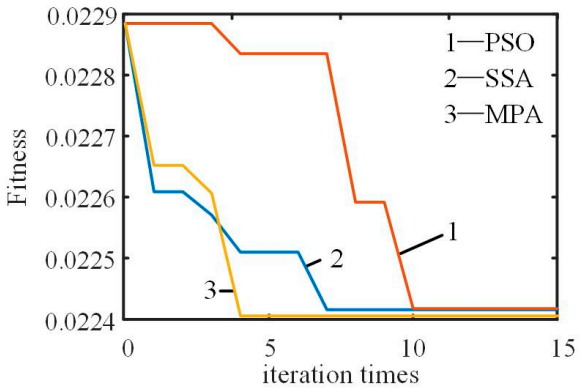


Figure 6. Comparison of results of different optimization algorithms.

From Figure 6, SSA demonstrated rapid initial convergence but showed susceptibility to local optima, reaching its optimal solution with a comprehensive entropy kurtosis ratio of 0.022424 by the seventh generation. PSO exhibited robust global search capabilities but slower convergence, achieving optimal solution with a comprehensive entropy kurtosis ratio of 0.022426 at the tenth generation. MPA combined quick convergence with effective global search, reaching optimal solution with a comprehensive entropy kurtosis ratio of 0.022410 by the fourth generation, surpassing both alternatives in optimization performance. In summary, MPA demonstrated superior optimization capabilities compared to PSO and

SSA. The application of MPA for MVMD parameter optimization significantly reduces result subjectivity while enhancing decomposition effectiveness.

Using MPA optimization, the optimal MVMD input parameters were determined as $(\hat{K},\hat{\alpha}) = (4, 2222)$. The resulting decomposition patterns for both line-mode and zero-mode traveling waves are presented in Figures 7 and 8.

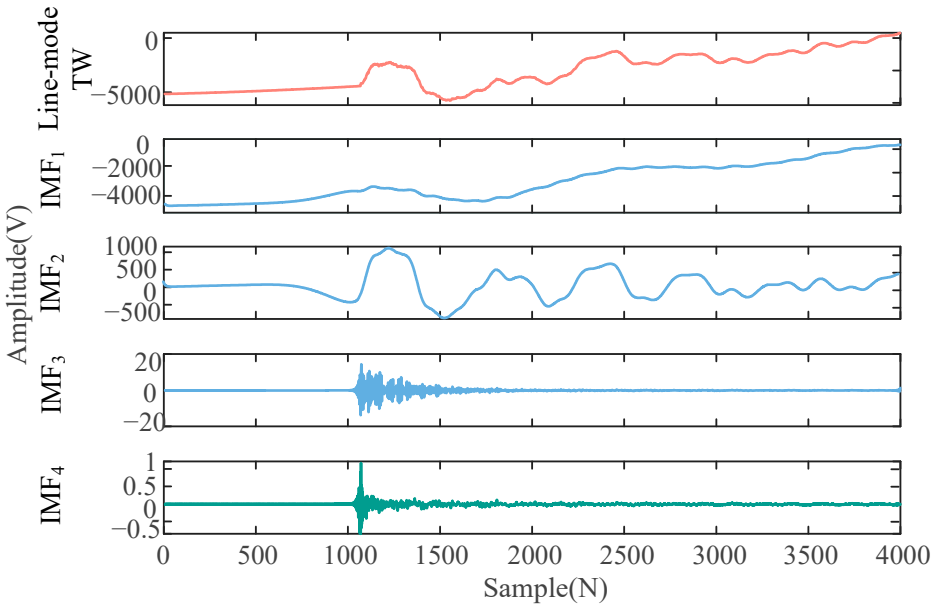


Figure 7. IMF$_m$ component of line-mode traveling wave.

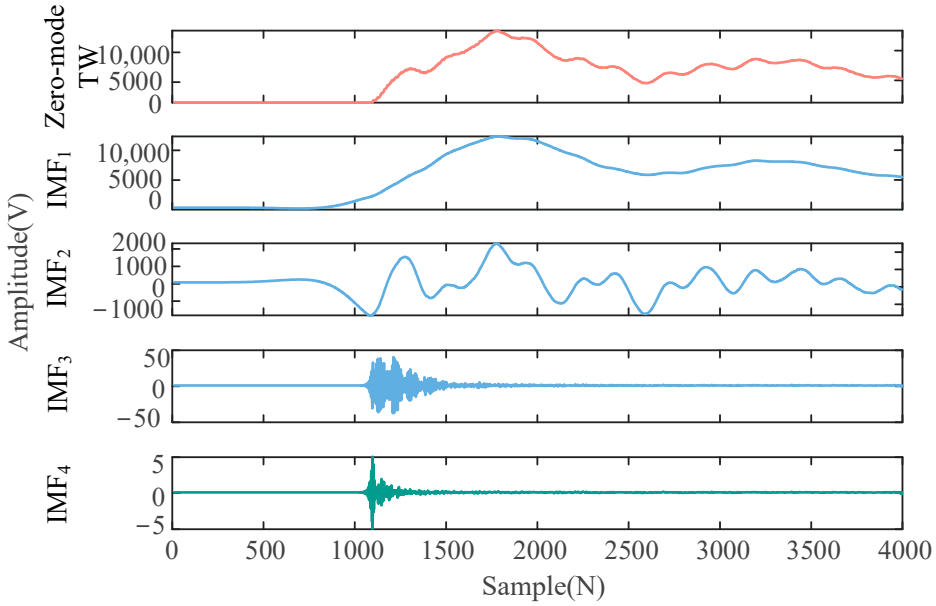


Figure 8. IMF$_m$ component of zero-mode traveling wave.

The entropy kurtosis ratios of IMF$_1$~IMF$_4$ in Figures 7 and 8 are calculated, and the results are shown in Tables 2 and 3.

Table 2. The entropy kurtosis ratio of IMF*m* of the line-mode traveling wave.

m	1	2	3	4
k_n	0.2809	0.1389	0.0163	0.0065

Table 3. The entropy kurtosis ratio of IMF*m* of the zero-mode traveling wave.

m	1	2	3	4
k_n	0.3865	0.2734	0.1721	0.0159

An analysis of Table 2 reveals that IMF_4 exhibits the lowest entropy kurtosis ratio, indicating that this component contains the most definitive traveling wave characteristics with minimal noise interference. Consequently, the line-mode's IMF_4 component is designated as its characteristic traveling wave signal. Similarly, Table 3 demonstrates IMF_4's minimal entropy kurtosis ratio for the zero-mode, leading to its selection as the zero-mode traveling wave characteristic signal. In Figures 7 and 8, the original waveform appears in red, the selected traveling wave characteristic signal (based on minimum entropy kurtosis ratio) in green, and the remaining IMF components are in blue. This color convention applies to all similar waveforms throughout this paper.

To precisely determine wave head arrival times for both line-mode and zero-mode traveling waves, morphological gradient analysis is applied to detect mutation points in the traveling wave characteristic signals. The results are illustrated in Figures 9 and 10.

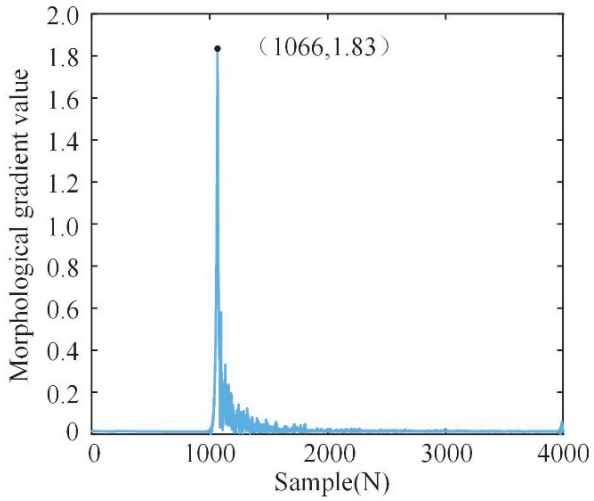


Figure 9. Line-mode traveling wave characteristic signal after morphological gradient processing in the first fault condition.

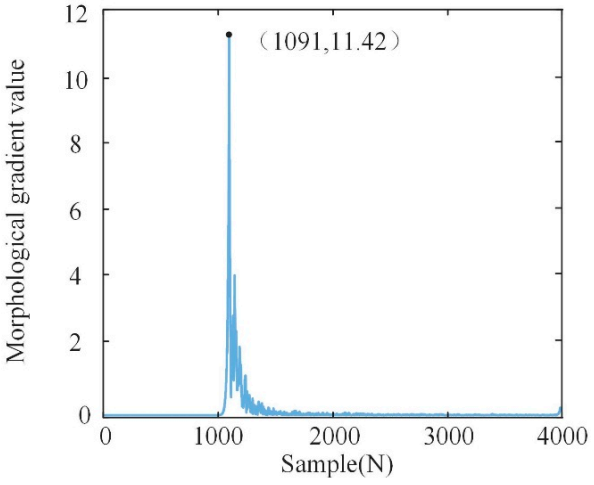


Figure 10. Zero-mode traveling wave characteristic signal after morphological gradient processing in the first fault condition.

The line-mode signal's morphological gradient reaches its peak at sampling point 1066, indicating maximum local amplitude variation. Given that sampling point 1000 corresponds to the fault initiation time of 0.135 s, the line-mode wave head arrives at the first measuring device at 0.135066 s.

For the zero-mode signal, the wave head reaches the first-end measuring device at 0.135091 s, establishing a 25 ms temporal difference between the line-mode and zero-mode arrival times. Applying Formula (22) yields a fault distance of 5.181 km with an absolute error of 19 m.

(2) A single-phase ground fault was simulated on hybrid line l_5, 4.2 km from section M, occurring at 0.1225 s with 100 Ω ground resistance and a 45° initial fault phase angle. The morphological gradient calibration results for both the line-mode and zero-mode traveling waves are presented in Figures 11 and 12.

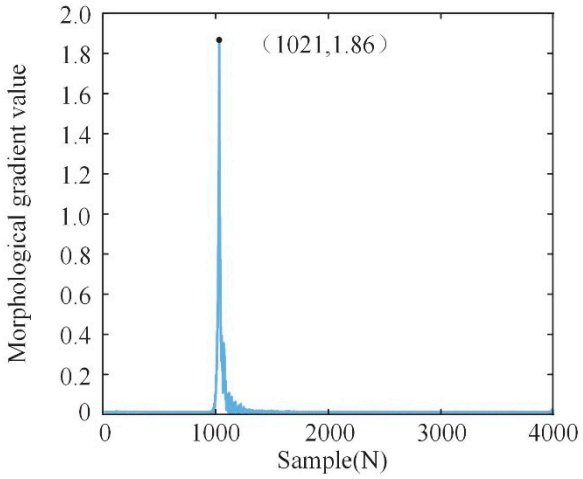


Figure 11. Line-mode traveling wave characteristic signal after morphological gradient processing in the second fault condition.

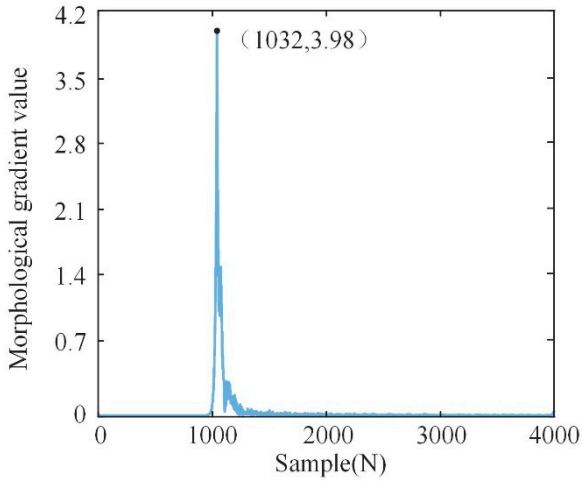


Figure 12. Zero-mode traveling wave characteristic signal after morphological gradient processing in the second fault condition.

It can be seen from Figures 11 and 12 that the line-mode traveling wave characteristic signal calibrated by the morphological gradient has a sudden change at sampling point 1021 and 0.122521 s, and the amplitude is the largest. The zero-mode traveling wave characteristic signal has a sudden change at sampling point 1032 and 0.122532 s, and the amplitude is the largest. The time difference between the arrival time of the line-mode

traveling wave and the zero-mode traveling wave is 11 ms. The fault distance is 4.223 km and the absolute error is 23 m, as calculated by Formula (25).

5.2. The Influence of Initial Fault Conditions

To evaluate the proposed method's robustness and accuracy, comprehensive testing was conducted across varying parameters: initial fault phase angle δ, transition resistance R, and fault distance d_a. Here, d_a represents the actual distance between the fault location and the primary terminal, d_m denotes the calculated fault distance using our proposed method, Δ indicates the absolute error margin, while t_1 and t_0 represent the arrival times of linear mode and zero-mode traveling wave heads, respectively.

In order to verify the influence of the neutral point grounding method on the positioning result, the cable line l_3 and the hybrid line l_5 are set to have a single-phase ground fault under the neutral point ungrounded mode and the neutral point grounded through the arc suppression coil. The positioning results are shown in Table 4.

Table 4. Fault location results under different neutral grounding modes.

Neutral Point Treatment	d_a/km	δ(°)	R/Ω	t_1/ms	t_0/ms	d_m/km	Δ/m
neutral point ungrounded	l_3-5 km	30	100	121.728	121.752	4.974	26
neutral point ungrounded	l_3-5 km	60	10	123.395	123.419	4.974	26
neutral point ungrounded	l_5-3 km	30	100	121.685	121.693	2.922	88
neutral point ungrounded	l_5-3 km	60	10	123.351	123.359	2.922	88
neutral earthing via arc extinguishing coil	l_3-5 km	30	100	121.728	121.752	4.974	26
neutral earthing via arc extinguishing coil	l_3-5 km	60	10	123.395	123.419	4.974	26
neutral earthing via arc extinguishing coil	l_5-3 km	30	100	121.685	121.693	2.922	88
neutral earthing via arc extinguishing coil	l_5-3 km	60	10	123.351	123.359	2.922	88

In order to verify the influence of fault type on the positioning results, different types of faults are set in cable line l_3 and mixed line l_5, and the positioning results are shown in Table 5.

Table 5. Fault location results under different fault types.

Fault Type	d_a/km	δ/(°)	R/Ω	t_1/ms	t_0/ms	d_m/km	Δ/m
A-G	l_3-5 km	30	100	121.728	121.752	4.974	26
A-G	l_5-3 km	30	100	121.685	121.693	2.922	88
A-B-G	l_3-5 km	30	100	121.728	121.752	4.974	26
A-B-G	l_5-3 km	30	100	121.685	121.693	2.922	88
A-C-G	l_3-5 km	30	100	121.728	121.752	4.974	26
A-C-G	l_5-3 km	30	100	121.685	121.693	2.922	88
B-C-G	l_3-5 km	30	100	121.728	121.752	4.974	26
B-C-G	l_5-3 km	30	100	121.685	121.693	2.922	88

To assess the impact of initial fault phase angle δ, single-phase ground faults were simulated at two locations: 1 km from section M on line l_3 and 5 km on line l_5. The tests were conducted at four distinct phase angles (10°, 30°, 60°, and 90°) with a constant transition resistance of 10 Ω. The results are documented in Table 6.

Table 6. Fault location results under different fault initial phase angle δ.

d_a/km	δ/(°)	t_1/ms	t_0/ms	d_m/km	Δ/m
l_3-1 km	10	120.569	120.574	1.036	36
l_3-1 km	30	121.680	121.685	1.036	36
l_3-1 km	60	123.347	123.352	1.036	36
l_3-1 km	90	125.013	125.018	1.036	36
l_5-5 km	10	120.583	120.597	4.989	11
l_5-5 km	30	121.694	121.708	4.989	11
l_5-5 km	60	123.361	123.375	4.989	11
l_5-5 km	90	125.027	125.041	4.989	11

The influence of fault transition resistance R was evaluated by introducing single-phase ground faults at 0.4 km from section M on line l_5 and 5.4 km from line l_3. The tests employed varying resistance values (10 Ω, 100 Ω, 500 Ω, and 1000 Ω) with a fixed initial fault phase angle of 90°. These findings are presented in Table 7.

Table 7. Fault location results under different fault transition resistances R.

d_a/km	R/Ω	t_1/ms	t_0/ms	d_m/km	Δ/m
l_5-0.4km	10	125.006	125.008	0.414	14
l_5-0.4 km	100	125.006	125.008	0.414	14
l_5-0.4 km	500	125.006	125.008	0.414	14
l_5-0.4 km	1000	125.006	125.008	0.414	14
l_3-5.4 km	10	125.067	125.093	5.388	12
l_3-5.4 km	100	125.067	125.093	5.388	12
l_3-5.4 km	500	125.067	125.093	5.388	12
l_3-5.4 km	1000	125.067	125.093	5.388	12

To examine the effect of fault distance d_a, single-phase ground faults were implemented at multiple locations: along line l_3 (0.4, 2.5, 3.3, and 6.2 km from section M) and line l_5 (0.4, 2.5, 3.3, and 5.2 km from section M). These tests maintained consistent parameters of 10 Ω transition resistance and 90° initial phase angle. The results are compiled in Table 8.

Table 8. Fault location results under different fault distances d_a.

Line Type	d_a/km	t_1/ms	t_0/ms	d_m/km	Δ/m
cable line l_3	0.4	125.006	125.008	0.414	14
	2.5	125.031	125.043	2.487	13
	3.3	125.041	125.057	3.316	16
	6.2	125.078	125.108	6.217	17
composite line l_5	0.4	125.006	125.008	0.414	14
	2.5	125.014	125.021	2.489	11
	3.3	125.018	125.027	3.356	56
	5.2	125.029	125.044	5.196	4

It can be seen from Tables 4 and 6–8 that the proposed method has high ranging accuracy under different neutral point treatments, fault initial phase angles, transition resistances, and fault distances. The maximum absolute error of the ranging result is 88 m. The size of the fault initial phase angle and fault distance only affect the amplitude of the wave head. The influence of the fault distance within the line length of the small current grounding system on the shape of the wave head is also very limited. Therefore, the accuracy of the positioning method in this paper is basically not affected by the initial conditions of the fault. However, it is mainly affected by the accuracy of the MVMD results. Due to the complexity of the decomposition process, the accuracy of the positioning method in this paper shows the law of uncertainty, which can also be seen from Tables 4–8.

In addition, it can be seen from Table 5 that the proposed method can accurately locate the fault location under single-phase grounding fault and two-phase grounding fault. However, for three-phase symmetrical grounding fault, three-phase fault, and two-phase fault, due to the absence of zero-mode component in the system, the method in this paper is invalid, and the scene is still worthy of further study.

5.3. The Influence of Noise

To evaluate our method's robustness against noise interference, the single-phase ground fault scenario from Section 5.1 on cable line l_3 is used for testing. Moreover, 20 dB noise is added to both the line-mode and zero-mode traveling waves originally shown in Figures 7 and 8. IMF$_m$ component of noisy line-mode traveling wave is shown in Figure 13. Line-mode traveling wave characteristic signal with noise after morphological gradient processing is shown in Figure 14. An analysis of the entropy kurtosis ratios revealed IMF$_1$ as the optimal component for both noise-contaminated waves, leading to their selection

as characteristic traveling wave signals. IMF$_m$ component of noisy zero-mode traveling wave is shown in Figure 15. Noisy zero-mode traveling wave characteristic signal after morphological gradient processing is shown in Figure 16.

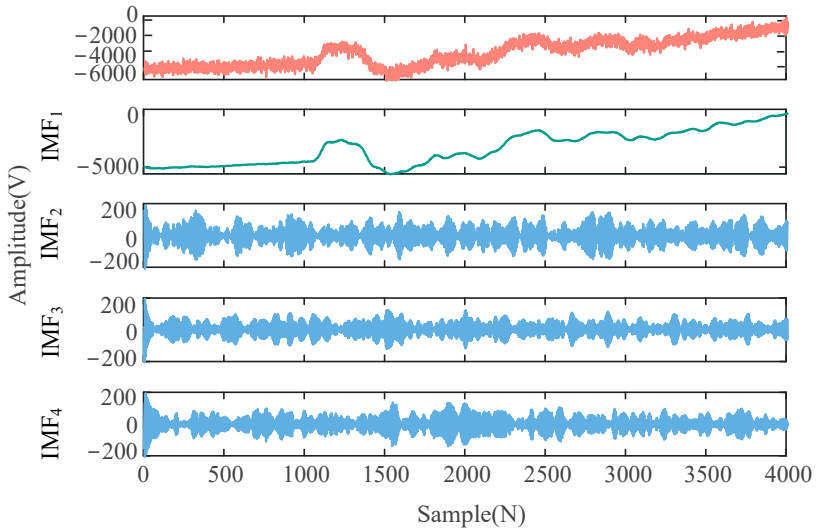


Figure 13. IMF$_m$ component of noisy line-mode traveling wave.

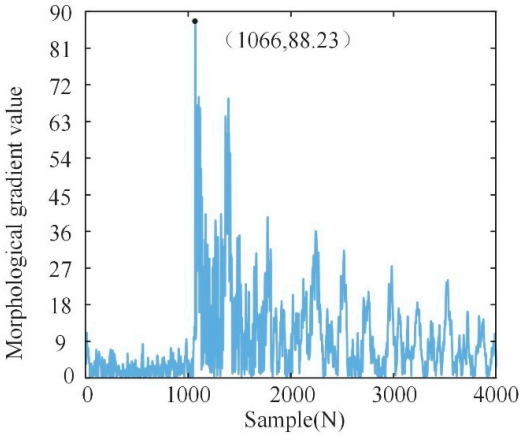


Figure 14. Line-mode traveling wave characteristic signal with noise after morphological gradient processing.

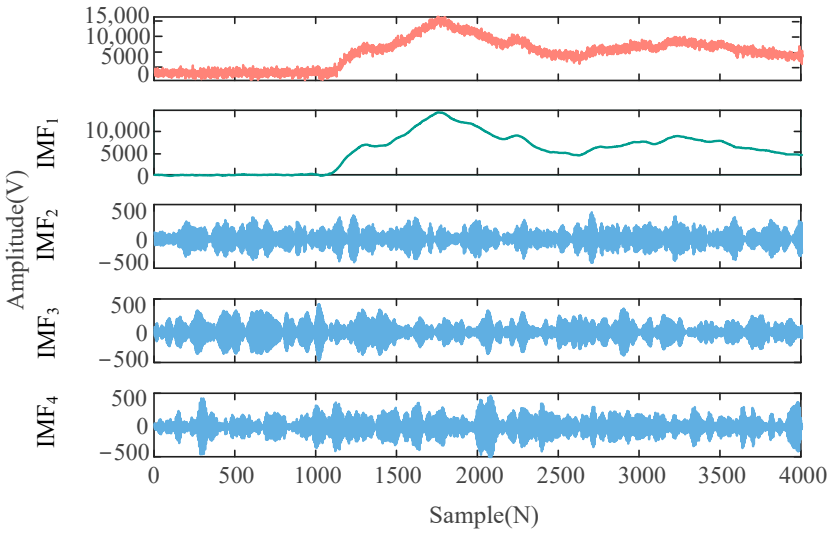


Figure 15. IMF$_m$ component of noisy zero-mode traveling wave.

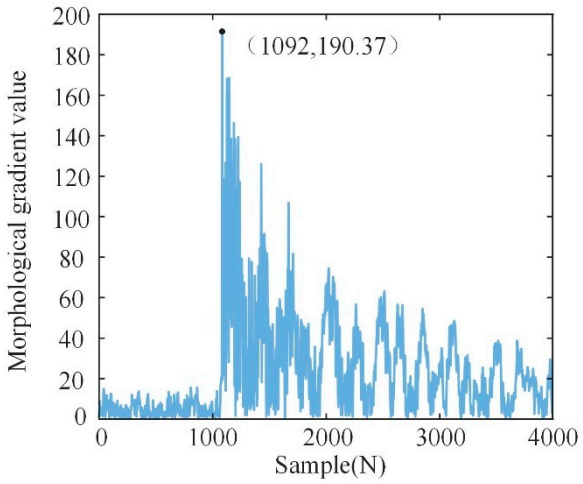


Figure 16. Noisy zero-mode traveling wave characteristic signal after morphological gradient processing.

An analysis of the noise-contaminated line-mode traveling wave depicted in Figures 13 and 15 reveals significant signal degradation, with the original wave pattern largely obscured by noise. However, the parameter-optimized MVMD method successfully extracts the characteristic traveling wave signal, preserving critical singularity features while effectively mitigating noise interference. The temporal difference between line-mode and zero-mode wave head arrivals is measured at 26 ms. The application of Formula (22) yields a fault distance of 5.388 km, resulting in an absolute error of 188 m.

Further validation tests were conducted on cable line l_3, with single-phase ground faults simulated at three distinct locations: 0.4 km, 3.2 km, and 5.2 km from section M. Test parameters included a fault initiation time of 0.135 s, 10 Ω grounding resistance, and 270° initial fault phase angle. Both line-mode and zero-mode traveling waves were subjected to varying noise levels (20 dB, 30 dB, and 40 dB). The fault localization results, presented in Table 9, demonstrate the method's robust performance under diverse noise conditions, confirming its strong resilience to noise interference.

Table 9. Fault location results under different noise interferences.

Noise/dB	d_a/km	d_m/km	Δ/m
0	0.4 3.2 5.2	0.414 3.108 5.181	14 92 19
40	0.4 3.2 5.2	0.414 3.108 5.181	14 92 19
30	0.4 3.2 5.2	0.622 3.108 5.388	222 92 188
20	0.4 3.2 5.2	0.622 3.316 5.388	222 116 188

5.4. Comparison of Different Algorithms

Taking the single-phase grounding fault at l_3 of the cable line in Section 5.1 as an example, the proposed method is compared with the VMD-TEO calibration method [23] and the EMD_first-order differential calibration method [24]. The algorithm time is shown in Table 10, and the positioning results are as follows:

Table 10. Times of different algorithms.

Parameter		Time/s		
		VMD-TEO	**EMD_First-Order Difference**	**MVMD-Morphological Gradient**
signal preprocessing	parameter optimization	0	0	1.2503
	mode decomposition	3.1632	0.4051	0.9104
traveling wave head calibration		0.0054	0.0036	0.0106
total time		3.1686	0.4087	2.1713

(1) VMD-TEO calibration method

Based on the principle of two-terminal ranging, VMD is used to decompose the two-terminal line-mode traveling wave. The number of modes and the penalty factor are set to 4 and 2000 according to human experience. The arrival time of the first IMF component is calibrated by TEO. The results of the double-end calibration are shown in Figures 17 and 18. The fault distance is calculated by using the traditional double-end ranging formula. The positioning result is 5.154 km and the absolute error is 36 m.

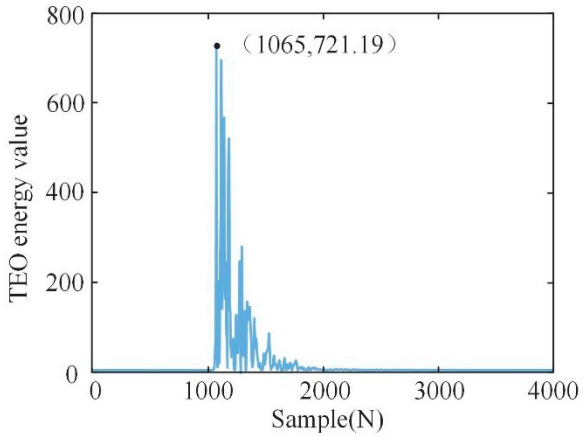


Figure 17. Arrival time of M section line-mode is calibrated by VMD-TEO method.

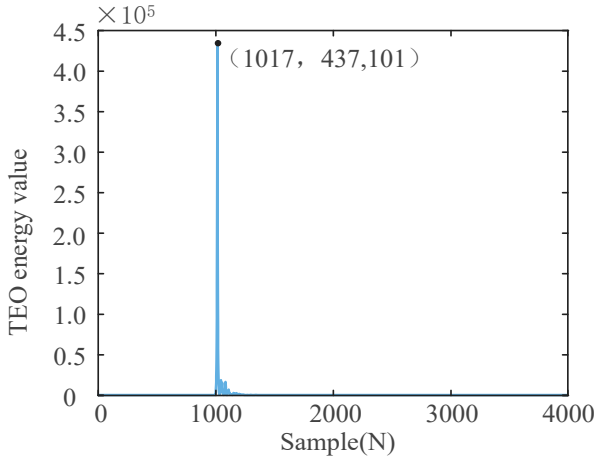


Figure 18. Arrival time of N section line-mode is calibrated by VMD-TEO method.

(2) EMD_first-order difference calibration method

Based on the principle of single-end wave velocity difference range, EMD is used to adaptively decompose line-mode traveling wave and zero-mode traveling wave, and the first-order difference algorithm is used to calibrate the arrival time of the highest frequency IMF component. The calibration results are shown in Figures 19 and 20. The ranging

distance is 5.388 km, and the absolute error is 188 m calculated by using the single-end mode velocity difference ranging formula.

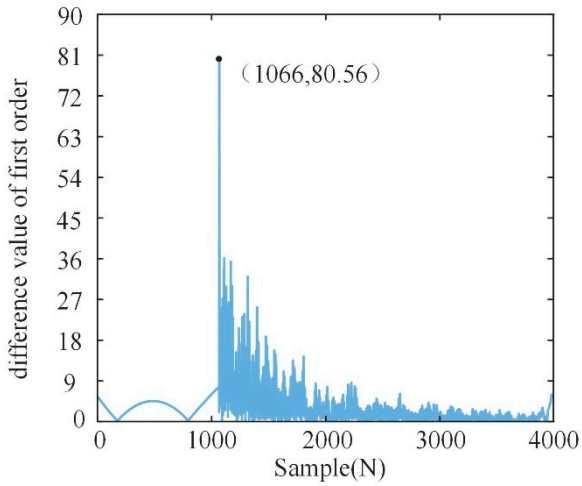


Figure 19. EMD_first-order difference calibration method is used to calibrate arrival time of M section line-mode.

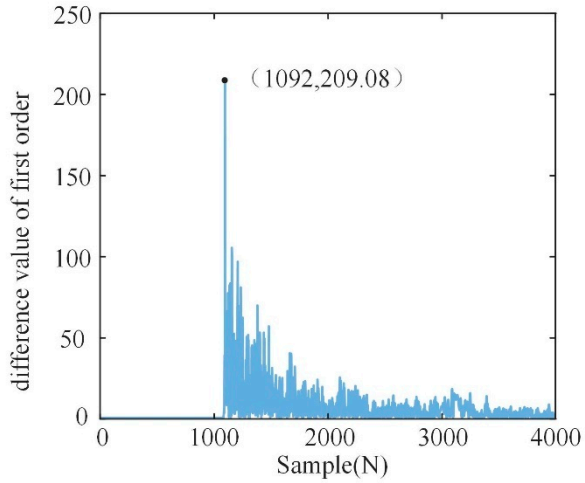


Figure 20. EMD_first-order difference calibration method to calibrate M section zero-mode arrival time.

The analysis of the positioning results is as follows:

(1) VMD-TEO sets the number of decomposition modes and penalty factors according to human experience, which fails to characterize the singularity of traveling wave signals to the greatest extent. In addition, the reliability of the method of selecting the highest frequency IMF component for wave head calibration is low. When the fault occurs at the far end of the line, the attenuation of the high frequency component is serious during the propagation process, and the noise interference is easily doped into the wave head. The singularity of the wave head in the high frequency component is further weakened, which has a great influence on the result of fault location.

(2) Although the EMD_first-order difference calibration method adaptively decomposes the traveling wave signal and overcomes the defect of artificially setting the decomposition parameters, the modal aliasing phenomenon is more serious, and the method of directly selecting the highest frequency IMF component for wave head calibration also has the problem of low reliability.

(3) In this paper, the optimal decomposition parameters of MVMD are determined by MPA, which effectively overcomes the shortcomings of human experience in setting decomposition parameters and retains the advantages of VMD, which is not affected by modal aliasing when extracting fault features. The morphological gradient algorithm enhances the singularity of the wave head to the greatest extent.

Among the three methodologies compared, our proposed approach achieves superior accuracy with an absolute error of just 19m. Table 8 reveals that while our method requires more processing time than the EMD_first-order difference approach, it demonstrates significant efficiency improvements over the VMD-TEO method. The simultaneous processing capability of MVMD for multi-channel signals enables concurrent analysis of line-mode and zero-mode traveling waves, substantially reducing characteristic signal extraction time compared to independent VMD processing.

To evaluate the influence of the noise, 20 dB noise is added to the line-mode traveling wave shown in Figure 7. The wave decomposition and calibration outcomes using the VMD-TEO method are presented in Figures 21 and 22, while the corresponding results for the EMD_first-order difference method are illustrated in Figures 23 and 24.

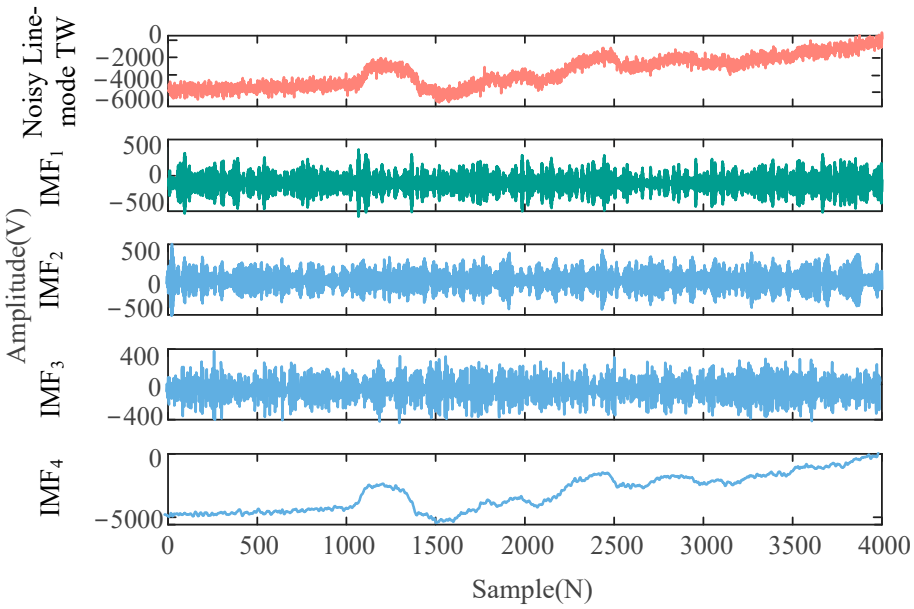


Figure 21. VMD decomposes the IMFm component of the traveling wave of the noisy line-mode.

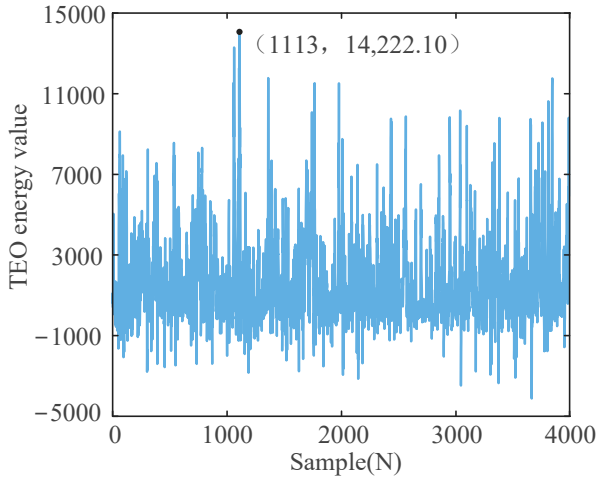


Figure 22. The highest frequency IMF component of noisy linear mode traveling wave after TEO processing.

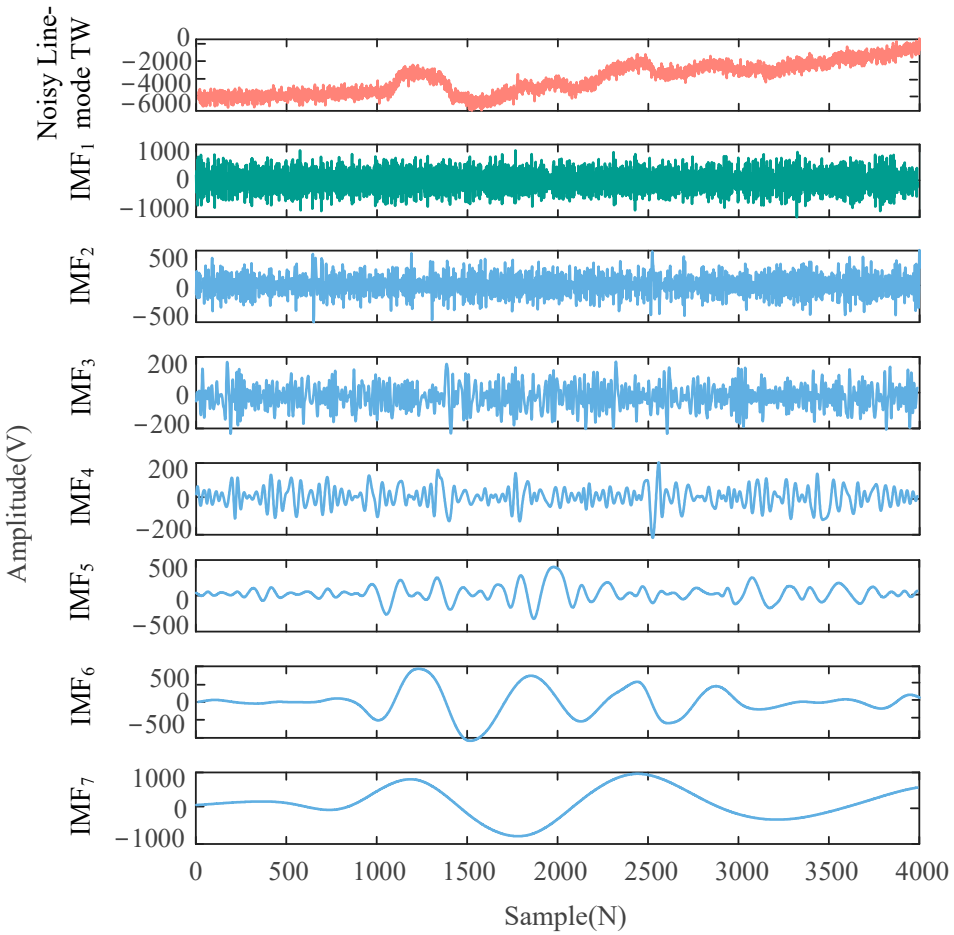


Figure 23. EMD of IMFm component of line-mode traveling wave with noise.

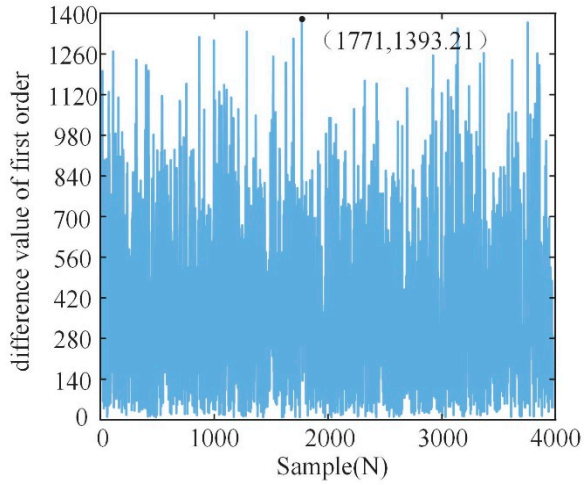


Figure 24. The highest frequency IMF component of the noisy line-mode traveling wave after first-order difference processing.

The green waveforms in Figures 21 and 23 are the traveling wave characteristic signal waveforms of each method. The wave head was completely submerged by noise in the highest frequency IMF component in the results of VMD and adaptive EMD based on human experience. It can be seen from Figures 22 and 24 that the VMD-TEO calibration method and the EMD_first-order differential calibration method are difficult to accurately calibrate the arrival time of the wave head, and the ranging fails. Under the same working

conditions, it can be seen from Section 5.3 that the positioning results of this method are less affected by noise.

6. Conclusions

In this paper, a single-end positioning method of modulus wave velocity difference based on MPA-optimized MVMD and morphological gradient is proposed. Through simulation and analysis, the following conclusions are obtained:

(1) Taking the minimum comprehensive entropy kurtosis ratio as the fitness function, the traveling wave characteristic signals with the most significant travel wave characteristic information and the lowest noise component can be decomposed. Then, the singularity of the wave head is further enhanced by the morphological gradient value, and the accurate location of the fault point is realized.

(2) Using MVMD to process both the line-mode traveling wave and zero-mode traveling wave at the same time can effectively shorten the extraction time of the traveling wave characteristic signals on the basis of retaining the advantages of VMD noise interference robustness without being affected by modal aliasing.

(3) The proposed method has strong adaptability to different types of line faults, different initial fault conditions, and noise interference. Compared with the VMD-TEO method and the EMD_first-order difference method, the accuracy of the positioning results of this method is the highest, and the algorithm time is significantly lower than that of the VMD-TEO method.

Author Contributions: Conceptualization, L.W. (Lingjie Wu); Methodology, Y.Z.; Validation, Y.W.; Formal analysis, J.C.; Data curation, Y.Z.; Writing—original draft, J.C.; Writing—review & editing, Y.W., L.W. (Lingjie Wu) and Y.Z.; Supervision, L.W. (Le Wang); Project administration, L.W. (Lingjie Wu) and L.W. (Le Wang); Funding acquisition, L.W. (Le Wang). All authors have read and agreed to the published version of the manuscript.

Funding: This research was funded by "the Fundamental Research Funds for the Central Universities (Ph.D. Top Innovative Talents Fund of CUMTB)". Grant number: BBJ2024066.

Data Availability Statement: The original data presented in this study are included in the manuscript. Further enquiries can be directed to the corresponding author.

Conflicts of Interest: Author Le Wang was employed by the company Datang North China Electric Power Test and Research Institute, China Datang Corporation Science and Technology General Research Institute Co., Ltd. The remaining authors declare that the research was conducted in the absence of any commercial or financial relationships that could be construed as a potential conflict of interest.

References

1. Qi, Z.; Hang, T.; Li, Y. Traveling Wave Fault Location for Arc-suppression Coil in Parallel with Low Resistance Grounding Mode. *Autom. Electr. Power Syst.* **2020**, *44*, 175–182.
2. Dong, L.; Xue, Y.; Li, J.; Pang, Q.; Li, B. Zero-sequence Voltage Distribution Characteristics and Location of Non-solidly Grounding Fault. *Autom. Electr. Power Syst.* **2022**, *46*, 180–187.
3. Peng, N.; Zhang, P.; Liang, R.; Guo, Z.; Hu, Y.; Li, W.; Sheng, Y. Fault location of three-core power distribution cables based on lump-parameter model considering conductor couplings. *Int. J. Electr. Power Energy Syst.* **2021**, *130*, 106953.
4. Doria-Garcia, J.; Orozco-Henao, C.; Iurinic, L.U.; Pulgarín-Rivera, J.D. High impedance fault location: Generalized extension for ground faults. *Int. J. Electr. Power Energy Syst.* **2020**, *114*, 105387.
5. Qiao, J.; Yin, X.; Wang, Y.; Xu, W.; Tan, L. An accurate fault location method for distribution network based on active transfer arc-suppression device. *Energy Rep.* **2021**, *7*, 552–560.
6. Chen, B.; Yu, N.; Chen, B.; Tian, C.; Chen, Y.; Chen, G. Fault Location for Underground Cables in Ungrounded MV Distribution Networks Based on ZSC Signal Injection. *IEEE Trans. Power Deliv.* **2021**, *36*, 2965–2977.

7. Naidu, O.-D.; Pradhan, A.-K. Precise Traveling Wave-Based Transmission Line Fault Location Method Using Single-Ended Data. *IEEE Trans. Ind. Inform.* **2021**, *17*, 5197–5207.
8. Deng, Z.; Zhang, F.; Pan, J.; Xu, Z.; Guo, Z.; Guo, L.; Wang, X. A New Method of Traveling Wave Ranging in Distribution Networks Based on the Difference between Zero-and Aerial-Mode Velocities. *Power Syst. Clean Energy* **2023**, *39*, 78–84.
9. Ren, X.; Pan, Y.; Hou, M.; Liang, R.; Su, L.; Wang, Q.; Zhang, P. Fault Location of the Renewable Energy Sources Connected Distribution Networks Based on Time Differences of the Modal Traveling Waves. *IEEE Access* **2023**, *11*, 129671–129682. [CrossRef]
10. Zhang, X.; Xu, C.; Ma, X.; Wang, Z.; Lin, D.; Lin, X.; Li, Z. Research on the precise fault location scheme for distribution network with multiple branches independent of time synchronization. *Power Syst. Prot. Control* **2019**, *47*, 56–63.
11. Abd el-Ghany, H.A.; Azmy, A.M.; Abeid, A.M. A General Travelling-Wave-Based Scheme for Locating Simultaneous Faults in Transmission Lines. *IEEE Trans. Power Deliv.* **2020**, *35*, 130–139. [CrossRef]
12. Xia, Y.; Li, Z.; Wang, S.; Sun, J.; Guo, X. Traveling wave inversion method of power line faults. *Int. J. Electr. Power Energy Syst.* **2023**, *149*, 109025. [CrossRef]
13. Xie, L.; Luo, L.; Li, Y.; Zhang, Y.; Cao, Y. A Traveling Wave-Based Fault Location Method Employing VMD-TEO for Distribution Network. *IEEE Trans. Power Deliv.* **2020**, *35*, 1987–1998. [CrossRef]
14. Wang, X.; Zhang, F.; Wei, X.; Gao, J.; Guo, L.; Wang, Y. Fault location of flexible grounding distribution system based on multivariate modes and kurtosis calibration. *Int. J. Electr. Power Energy Syst.* **2023**, *150*, 109108. [CrossRef]
15. Li, J.; Wang, G.; Luo, J.; Wang, Y.; Zhang, X.; Wang, X.; Wang, X. A Cable Fault Location Method of Distribution Networks Based on MVMD and Kurtosis Calculation. *Power Syst. Clean Energy* **2024**, *40*, 92–98.
16. Rehman, N.-u.; Aftab, H. Multivariate Variational Mode Decomposition. *IEEE Trans. Signal Process.* **2019**, *67*, 6039–6052. [CrossRef]
17. Zhao, F.; Wang, Y.; Wang, Y.; Chen, X. Multi-channel Sub-synchronous Oscillation Mode Identification of Direct-drive Wind Turbines Based on Improved MVMD and SOBI Algorithms. *High Volt. Eng.* **2022**, *48*, 1365–1374.
18. Faramarzi, A.; Heidarinejad, M.; Mirjalili, S.; Gandomi, A.H. Marine Predators Algorithm: A nature-inspired metaheuristic. *Expert Syst. Appl.* **2020**, *152*, 113377. [CrossRef]
19. Li, Z.-j.; Zhang, H.-p.; Wang, Y.-n.; Li, X. Wavelet threshold denoising harmonic detection method based on permutation entropy-CEEMD decomposition. *Electr. Mach. Control* **2020**, *24*, 120–129.
20. Wang, X.; Wei, X.; Gao, J.; Song, G.; Kheshti, M.; Guo, L. High-Impedance Fault Detection Method Based on Stochastic Resonance For a Distribution Network With Strong Background Noise. *IEEE Trans. Power Deliv.* **2022**, *37*, 1004–1016. [CrossRef]
21. Zhou, F.; Xiao, S.; State Key Laboratory of Alternate Electrical Power System With Renewable Energy Sources (North China Electric Power University). Grounding Fault Location of Active Distribution Network Based on Zero Sequence Current Distribution. *Power Syst. Technol.* **2022**, *46*, 1820–1832.
22. Liu, Z.; Shu, Q.; Han, X.; Huang, H. An iterative fault location algorithm using the difference of wave velocity between zero mode component and aerial mode component of traveling wave. *Power Syst. Prot. Control* **2015**, *43*, 88–93.
23. Pang, Q.-l.; Ye, L.; Ma, Z.-x.; Zheng, Y. Traveling Wave Fault Location of Multi-branch Small Current Grounding System Based on VMD-TEO. *Sci. Technol. Eng.* **2022**, *22*, 11943–11950.
24. Wang, J.; Zhang, Y. Traveling Wave Propagation Characteristic-Based LCC-MMC Hybrid HVDC Transmission Line Fault Location Method. *IEEE Trans. Power Deliv.* **2022**, *37*, 208–218. [CrossRef]

Disclaimer/Publisher's Note: The statements, opinions and data contained in all publications are solely those of the individual author(s) and contributor(s) and not of MDPI and/or the editor(s). MDPI and/or the editor(s) disclaim responsibility for any injury to people or property resulting from any ideas, methods, instructions or products referred to in the content.